https://www.sciencedirect.com/science/article/pii/S0997754617301577
https://doi.org/10.1016/j.euromechflu.2017.09.003

Lattice Boltzmann simulations of gravity currents

L. Ottolenghi[a,*], P. Prestininzi[a], A. Montessori[a], C. Adduce[a], M. La Rocca[a]

[a] *Department of Engineering, University of Roma Tre, Rome, 00146, Italy*

Abstract

This paper is aimed at assessing the ability of the Lattice-Boltzmann Method (LBM) in reproducing the fundamental features of lock-exchange gravity currents. Both two- and three-dimensional numerical simulations are presented at different Reynolds numbers ($1000 \leq Re \leq 30000$). Turbulence has been accounted for by implementing an equivalent Large Eddy Simulation (LES) model in the LBM framework. The advancement of the front position and the front velocity obtained by LBM numerical simulations are compared with laboratory experiments appositely performed with similar initial and boundary conditions and with previous results from literature, revealing that the dynamics of the gravity current as a whole is correctly reproduced. Lobes and clefts instabilities arising in three-dimensional simulations and the entrainment parameter are also analysed and comparisons with previous studies are presented.

Keywords: Buoyancy-driven flows, Computational methods in fluid dynamics, Lattice-Boltzmann Method,

*Corresponding author
Email addresses: luisa.ottolenghi@uniroma3.it (L. Ottolenghi), claudia.adduce@uniroma3.it (C. Adduce), michele.larocca@uniroma3.it (M. La Rocca)

Preprint submitted to European Journal of Mechanics B/Fluids *July 4, 2017*

PACS: 47.55.P-, 47.11.-j, 47.11.Qr, 05.10.a

1. Introduction

Gravity currents are generated by density gradients. The buoyancy force drives the motion, which develops primarily in the horizontal direction. Temperature or concentration gradients cause density-driven gravity currents, such as thermal circulation in lakes or salt wedge at estuarine zones, while suspended sediments give rise to particle-driven gravity currents, such as turbidity currents, snow avalanches or pyroclastic flows [1]. Gravity currents are important and complex phenomena, with relevant implications in both natural and anthropic flows: for this reason they have been extensively investigated by laboratory experiments and numerical simulations, resorting to simplified models as the constant-flow and lock-exchange techniques [2, 3, 4]. In order to perform numerical simulation of unsteady gravity currents, realized by means of the lock-exchange technique, different numerical approaches have been used. Many of these approaches adopt the shallow water hypothesis and are able to give a simplified but technically satisfying description of the flow, mainly concerned with the advancement of the front position and the shape of the gravity current. These shallow water models can take quite easily into account complex issues, as the entrainment of ambient fluid and the frictional effects on the bottom [5, 6, 7, 8]. The detailed description of the gravity current is obtained by means of high-resolution numerical simulations, based on the Navier-Stokes equation, with the Boussinesq approximation. Both the Direct Numerical Simulation (DNS) and the Large Eddy Simulation (LES) approaches have been applied successfully, revealing the main features of the flow in different settings. In the studies of [9, 10, 11] DNS were presented together with detailed analysis of the flow topology and the front velocity, with particular attention to the head region of the dense current and to the flow instabilities developing in this zone. LES of lock-release gravity currents at different Reynolds numbers propagating on a smooth bed and on a periodic array of obstacles were performed by [12] and [13], respectively, and an extensive description of energy budgets, drag and lift forces was given. In [14] mixing and entrainment in unsteady gravity currents with different initial excess density and different aspect ratio of the released volume were analysed by LES. The dynamics of density currents flowing down an incline were discussed in the works of [15, 16, 17] who performed two-dimensional and three-dimensional DNS, while in [18, 19] LES of gravity currents propagating up a sloping bottom were analysed in terms of front advancement, mixing and entrainment, and near-bed dynamics.

An alternative to these models based on the continuum assumption, is given by the Lattice Boltzmann Method (LBM), defined in the framework of the kinetic theory, which describes the flow in terms of Probability Density Functions (PDF). The macroscopic flow quantities, i.e. flow density and velocity, are obtained as zero-th and first order statistical moments of the PDFs [20]. The intrinsic simplicity and versatility of the LBM determined its tremendous development in the Computational Fluid Dynamics field [21]. The first successful attempt of LBM simulation of density driven flows, was made by [22], who considered simple cases of two-dimensional thermal natural convection, adopting the Boussinesque's hypothesis in the Navier-Stokes framework. The first application of the LBM to gravity currents was performed in [23, 24, 25], where different LBM formulations were developed in the framework of the shallow water theory. The latter gives a technical description of the gravity current, i.e. in terms of vertically average velocities and current's depth. The results obtained from the LBM formulation of the shallow water theory, mainly regarding the gravity current's front propagation characteristics and development phases, agree very well with those obtained directly from the shallow water theory ([23]). Moreover, the LBM formulation of the shallow water theory benefits from the intrinsic versatility of the LBM formulation, as shown in [24], where the interaction of the gravity current with an obstacle is considered.

To the authors' best knowledge, a LBM formulation equivalent to the Navier-Stokes equation with the Boussinesq approximation, has not yet been implemented and applied to the numerical simulation of lock-exchange gravity currents.

This paper is then aimed at assessing the ability of the LBM formulation equivalent to the Navier-Stokes equation with the Boussinesq approximation in reproducing the fundamental features of the dynamics of an unsteady gravity current, realised by means of the lock-exchange technique. Particular attention is paid to the simulation of the slumping and self-similar phases of the gravity current [26]. Both two-dimensional (2D) and three-dimensional (3D) numerical simulations are performed. Four different Reynolds number are considered ($Re = 1000, Re = 5000, Re = 10000, Re = 30000$) in order to span from mildly unstable viscous density currents to fully developed three-dimensional turbulent flows. Turbulence modelling is taken into account by means of a peculiar modification of the basic LBM [27], which makes it equivalent to the LES. Furthermore, laboratory experiments were performed and used as benchmark to the numerical results. The agreement between numerical and experimental results is satisfying, then revealing that the fundamental features of the dynamics of the gravity current are correctly reproduced.

The paper is organized as follows: In section 2 the LBM for density driven flows is presented; in section 3 relevant dimensionless numbers and the parameters used for the implementation of the model are introduced; in section 4 the experimental set-up used for the laboratory experiments is described; the results are presented and discussed in section 5, while conclusions are given in section 6.

2. The Lattice Boltzmann Method for density driven flows

The lattice Boltzmann method is based on a minimal (lattice) version of the Bhatnagar-Gross-Krook equation, in which the computational molecules stream along the links of a uniform lattice, and collide on the nodes according to a simple relaxation to a local equilibrium. For a comprehensive derivation of the method the reader is referred to [21], with particular attention to its supplementary material. In equations:

$$f_i(\mathbf{x} + \mathbf{c_i}\Delta t, t + \Delta t) = f_i(\mathbf{x}, t) + \frac{\Delta t}{\tau}\left(f_i^{eq} - f_i(\mathbf{x}, t)\right) + \frac{\Delta t}{c_s^2}\mathbf{c}_i \cdot \mathbf{F} \qquad (1)$$

where $f_i(\mathbf{x}, t)$ is the discrete distribution function, representing the probability of finding a particle at position $\mathbf{x}$ and time t with discrete velocity $\mathbf{c}_i$, being i the index spanning over the lattice discrete directions, $i = 0, .., b$, [28]. Finally, Δt is the lattice time step. The left-hand side of the equation (1) represents the free-streaming of particles within the lattice, which hop from a lattice node to neighbor ones according to the direction defined by the lattice vector $\mathbf{c_i}$. The right-hand side includes the forcing term and the collisional relaxation of the set of distribution functions towards the discrete local equilibria f_i^{eq}, i.e. truncated low-Mach number expansion of the Maxwell-Boltzmann distribution, which reads as follows:

$$f_i^{eq} = w_i \rho \left[1 + \frac{(\mathbf{c}_i \cdot \mathbf{u})}{c_s^2} + \frac{(\mathbf{c}_i \cdot \mathbf{u})^2}{2c_s^4} - \frac{\mathbf{u} \cdot \mathbf{u}}{2c_s^2} \right] \tag{2}$$

where w_i are weights of the discrete equilibrium distribution functions, c_s is the lattice sound speed, $\mathbf{u}$ is the macroscopic flow velocity. The parameter τ in equation (1) is the relaxation time which controls the lattice kinematic fluid viscosity through the relation, [28]:

$$\nu = c_s^2 \left(\tau - \frac{1}{2} \right) \tag{3}$$

In this work, we shall use two classes of lattices, the D2Q9 and the D3Q19, both 4^{th} order isotropic in two and three dimensions, respectively (see Fig. 1). The standard notation DnQm for m discrete velocities in n spatial dimensions is used throughout. The weights coefficients w_i depend on the considered lattice. For the D2Q9 lattice are defined as:

$$\begin{aligned} w_0 = & \quad 4/9 \ (i = 0) \\ w_i = & \quad 1/9 \ (i = 1, ..., 4) \\ w_i = & \quad 1/36 \ (i = 5, ..., 8) \end{aligned} \tag{4}$$

while the D3Q19 lattice are defined as:

$$\begin{aligned} w_0 = & \quad 1/3 \ (i = 0) \\ w_i = & \quad 1/18 \ (i = 1, ..., 6) \\ w_i = & \quad 1/36 \ (i = 7, ..., 18) \end{aligned} \tag{5}$$

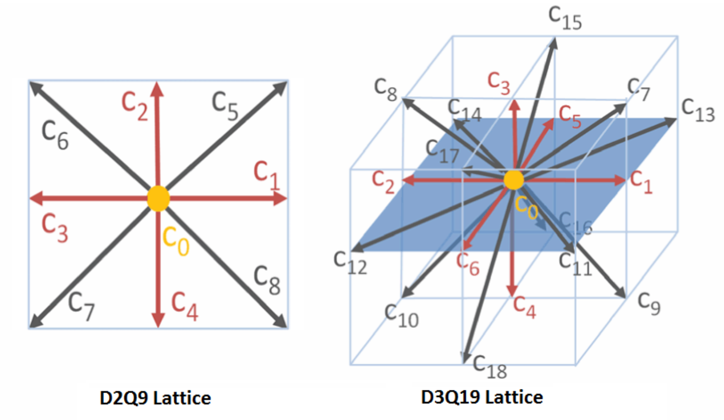

Figure 1: 2DQ9 and 3DQ19 Lattices

The relevant hydrodynamic macroscopic quantities, i.e. density, linear momentum and momentum flux tensor, are given by statistical moments of the distribution functions:

$$\rho(\mathbf{x}, t) = \sum_i f_i(\mathbf{x}, t) \tag{6}$$

$$\rho\mathbf{u}(\mathbf{x}, t) = \sum_i f_i(\mathbf{x}, t)\mathbf{c}_i \tag{7}$$

$$\underline{\Pi}(\mathbf{x}, t) = \sum_i f_i(\mathbf{x}, t)\underline{Q}_i \tag{8}$$

where $\underline{Q}_i = \mathbf{c}_i\mathbf{c}_i - c_s^2\underline{I}$, $\underline{I}$ being the identity matrix.

According to the Boussinesq's approximation [29], if the relative density variation is small ($\frac{\Delta\rho}{\rho} << 1$), as in the case of gravity currents due to salinity gradients in natural environments, the fluid can be considered as incompressible and the variation of density is retained only in the gravity force term:

$$\mathbf{F} = -\rho_m(\mathbf{x}, t)g\ \hat{k} \tag{9}$$

where $\hat{k}$ is the unit vector defining the vertical direction (upwardly oriented) and ρ_m is the density of the mixture which can be expressed as:

$$\rho_m(\mathbf{x}, t) = \rho\,(1 + \beta C(\mathbf{x}, t)) \tag{10}$$

being ρ the density of the ambient fluid (the fresh water) and $C(\mathbf{x}, t)$ the volumetric concentration. $\beta = (\rho_s - \rho)/\rho$ with ρ_s the solute's density. It can be shown [30] that equations (1), together with the definition of the external force (10), the equilibrium PDF (2) and the macroscopic quantities (8) are equivalent to the mass conservation and the Navier-Stokes equation, with the Boussinesq's forcing term:

$$\begin{aligned} \nabla \cdot \mathbf{u} &= 0 \\ \frac{\partial \mathbf{u}}{\partial t} + \mathbf{u} \cdot \nabla \mathbf{u} &= -g(1 + \beta C)\mathbf{k} - \frac{\nabla p}{\rho} + \nu^* \nabla^2 \mathbf{u} \end{aligned} \tag{11}$$

In other words, equations (11) can be obtained expanding the probability density functions f_i in equations (1), assuming the Knudsen number Kn as small parameter. The latter is defined as the ratio of the mean free path $\lambda = \nu/c_s$ to a macroscopic length of the flow H and can be expressed as:

$$Kn = \frac{\lambda}{H} = \frac{\nu}{c_s H} = \frac{\nu}{UH}\frac{U}{c_s} = \frac{Ma}{Re} \tag{12}$$

being U the macroscopic velocity scale. Re, Ma are respectively the Reynolds and the Mach number of the flow ($Re = \frac{UH}{\nu}, Ma = \frac{U}{c_s}$). Equations (1) are equivalent to equations (11) if the Knudsen number is small ($Kn << 1$). For turbulent flows, such as the ones considered in this paper, the use of turbulence closure models is mandatory in order to contain the computational resources. In this paper a peculiar modification of the basic LBM, equivalent to a Large Eddy Simulation (LES) closure based on the Smagorinsky formulation of subgrid turbulence stresses, is employed [27].

In the filtered LES-LB equation, the effect of the unresolved scale motion is modelled through an effective collision relaxation time scale $\tau_* = \tau + \tau_t$, being τ the relaxation time controlling the kinematic viscosity of the model through the relation reported in Eq. 3 and τ_t the so-called eddy relaxation time. If the Smagorinsky closure is employed, the eddy viscosity ν_t, which is used to compute the turbulence relaxation time τ_t, is computed from the filtered strain rate tensor as follows:

$$\nu_t = (C_S \Delta_x)^2 \underline{S} \tag{13}$$

$$\underline{S} = \frac{\underline{\Pi}}{2c_s^2 \tau_*}, \quad \underline{\Pi} = \sqrt{2 \sum_{i,j} \underline{\Pi_{i,j}}\ \underline{\Pi_{i,j}}} \tag{14}$$

In the equations above, $\underline{S}$ and $\underline{\Pi}$ are the filtered rate of strain rate and the filtered mean momentum flux, respectively. C_S is the Smagorinsky constant and $\Delta_x = \Delta x = 1$ is the characteristic filter length scale. Once the strain rate tensor is computed and the C_S fixed, the eddy relaxation time τ_t can be computed from equation (13) and the collision step is then performed with the effective local relaxation time τ_*. It is worth noting, that the filtered momentum flux can be locally computed as the second-order statistical moment of the off-equilibrium part of the set of distribution functions. Thus, even the filtering step retains the local features of the LB, not requiring the computation of any macroscopic derivative.

In order to simulate the advection-diffusion of the concentration C, needed to close the formulation (11), a second set of PDF is introduced, namely χ_i.

Its evolution is governed by the LBM algorithm:

$$\chi_i(\mathbf{x} + \mathbf{c_i}\Delta t, t + \Delta t) = \chi_i(\mathbf{x}, t) + \frac{1}{\tau_\chi}\left(\chi_i^{eq} - \chi_i(\mathbf{x}, t)\right) \tag{15}$$

for $i = 0, 1, ..., N$, where N is the number of allowed velocities in the chosen velocity set. In this study the velocity set is chosen to be identical to the one employed by the hydrodynamic solver; τ_χ is the dimensionless relaxation time for the concentration, while χ_i^{eq} is the equilibrium PDF for the concentration, relative to the i^{th} direction of the lattice. The expression of χ_i^{eq} is identical to Eq. (2), with C instead of ρ. The flow velocity appearing in χ_i^{eq} is the one given by the hydrodynamic model: this, together with the forcing term Eq. (9) constitute the full coupling between the two models. The concentration C is then obtained as zeroth order statistical moment of χ:

$$C = \sum_{i=0}^{N} \chi_i \tag{16}$$

Equation (15), together with the definition of the equilibrium PDFs and the equation (16) is equivalent to the advection diffusion equation for the concentration:

$$\frac{\partial C}{\partial t} + \mathbf{u} \cdot \nabla C = \kappa \nabla^2 C \tag{17}$$

where κ is a diffusion coefficient, defined as:

$$\kappa = c_s^2 \left(\tau_\chi - \frac{1}{2}\right) \tag{18}$$

3. Scaling and computational aspects

The considered configuration is the full-depth lock-exchange experiment [1], which, at the initial instant of time $t = 0$, consists of a parallelepiped

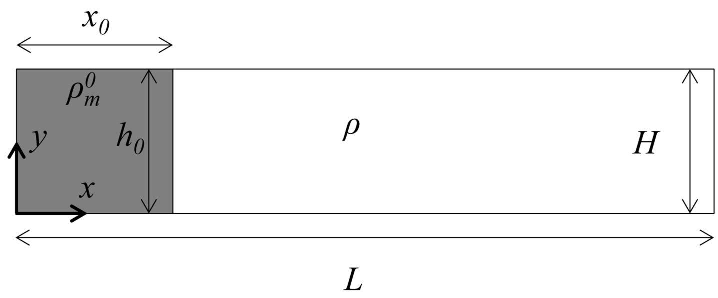

Figure 2: Sketch of the lock-exchange experiment

tank $L \times H \times W$, divided into two parts by a vertical removable wall (figure 2) placed at $x = x_0$. The two parts are filled respectively with heavy fluid with density ρ_m^0 for $0 < x \leq x_0$, and with ambient fluid with density $\rho < \rho_m^0$, for $x_0 < x \leq L$. The aspect ratio of the lock R is defined as: $R = H/x_0$. Upon removal of the vertical wall, the two fluids interact and a gravity current develops: the denser fluid flows on the bottom of the tank, beneath the ambient fluid, driven by the horizontal pressure gradient. The lock-exchange configuration considered in this paper is reported in Table 1.

In order to set up the LBM simulations, a proper scaling has to be determined and the relevant non dimensional groups matched. As usual in buoyancy phenomena, the Rayleigh ($Ra = g\beta\Delta C l^3/(\nu\kappa)$) number fully describes the dynamics, being l a reference length scale. Moreover, the Schmidt ($Sc = \nu/\kappa$) number measures momentum to solute diffusion. Since Sc is commonly set to unity [9, 31, 32], Ra reduces to Grasshof ($Gr = Ra/Sc$). In addition, if one chooses the reference length l as the initial depth in the lock H and the reference velocity as the so called buoyancy velocity $U = \sqrt{g'H}$, where $g' = g\beta\Delta C$ is the reduced gravity, Ra can be expressed as a function of Re. Ra reads:

$$Ra = \frac{g\beta\Delta C H^3}{\nu^2} \equiv Re^2 \tag{19}$$

The grid spacing, identified by the value of H, is chosen to be sufficient to represent the boundary layer, avoiding the use of wall layer models. Specifically, it was a posteriori verified that the dimensionless grid size was such that $\Delta y^+ < 2$ at the bottom, where Δy^+ is the grid spacing made non-dimensional by u_τ/ν, with u_τ the friction velocity.

In order to match the desired Re, the relaxation parameter is calculated by means of Eq. (3) as $\tau = 1/2 + \nu/c_s^2$, since $\nu = Re\sqrt{g'H^3}$. The only degree of freedom left is the value of the reduced gravity, which can be tuned to stabilize the code: within the range of stability no difference is experienced in the results. Its value is set to $g' = 10^{-4}$ for all simulations. It is clear from the above scaling that, once the Re has been matched, any value for ΔC would yield the same results: in all simulation ΔC was set to unity.

Initial values for f_i and χ_i were chosen as the corresponding equilibrium PDFs. As for the hydrodynamic boundary conditions, no-slip Boundary Conditions (BCs) are set at all boundaries but the top, where a free-slip BC is imposed. For what regards the concentration, zero-gradient BCs are imposed everywhere. Within the LBM framework, the hydrodynamics no-slip and free-slip BCs are obtained by means of the so called bounce-back and bounce-forward rules, respectively, for which a second order formulation in space and time is implemented in our code [33]. If applied to the distributions of concentration, namely χ_i, the bounce-back rule reproduces the required zero-gradient condition.

For what regards the computational burden required, LBM has proven to be

Table 1: Numerical simulations. All length quantities are expressed in Lattice Units (LU)

NAME	Re	R	$H(LU)$	L/H	W/H
Re1-2D	1000	1	90	30	0
Re5-2D	5000	1	261	30	0
Re10-2D	10000	1	431	10	0
Re30-2D	30000	1	504	10	0
Re1-3D	1000	1	66	20	1
Re5-3D	5000	1	39	30	1
Re10-3D	10000	1	66	30	1

exceptionally agile [34, 35]. The basic algorithm consists of extremely simple calculations of collided distributions and their successive shift in memory. The key point here is the abscence of any need to perform any kind of differentiation, at least in the basic streaming-collision-moments procedures. The resulting locality in memory provides LBM with parallel scaling properties unprecedented in numerical fluid-dynamics [36, 37], particularly suited for exploiting the full potential of modern architectures [38, 39, 40, 41]. The only drawback is the amount of memory required, being roughly 3-5 times larger than classical approaches based on discretization of continuous equations. The resulting algorithms are thus mainly limited memory bandwidth [42]. The "home made" code employed here, which features a simple shared-memory OpenMP parallelization, scales poorly already above 4-5 cores. The computational times for the simulations carried out in this study range from 1 to 5 days on 6 cores desktop machines. These timings are far to be considered as accurate measures of the LBM algorithm capability, as they strongly depend on coder's ability, algorithm implementations, compiler's settings, etc.

4. Experimental Setup

Laboratory experiments were performed at the Hydraulics Laboratory of "Roma Tre" University. A plexiglas tank with $L = 3$ m, $W = 0.2$ m and maximum depth $H_{max} = 0.3$ m was used to perform the experiments. The channel was filled for $0 \leq x \leq x_0$ with salty water (density ρ_m^0) and for $x_0 < x \leq L$ with tap water with density ρ. The corresponding β is equal to: $\beta = 1.16$. The desired Reynolds number (Table 2) was obtained by setting a suitable height of the lock H and, for the low Reynolds cases ($Re = 1000, Re = 5000$) by adding small quantities of Glycerol [43]. Dye (E171, titanium dioxide) was added to the dense fluid in order to ensure the visibility of the gravity current. A CCD video camera with a resolution of 768 x 576 pixels and an acquisition frequency of 25 Hz was used to record the experiments. Black and white images were then analysed and converted in matrices of grey levels, with an accuracy related to the resolution of the recording camera (~ 2 mm). The density field was inferred from dye concentration calibrating each pixel with images with a known concentration of uniformly distributed dye acquired at the end of the experiment [as in 44, 14, 18].

Experimental images captured by the camera during the laboratory experiments are shown in Fig. 3 for the different Re tested. In the figure, changes in behaviour of the gravity currents with varying Re are clearly visible, with an increase of the flow complexity and the development of turbulent patterns with the increase of Re.

Table 2: Laboratory experiments.

NAME	Re	H	g'_0	ν	l_{vis}/x_0
E-Re1	1000	0.08	0.125	6.804 10^{-6}	7.5
E-Re5	5000	0.08	0.140	1.731 10^{-6}	11
E-Re10	10000	0.08	0.193	1.000 10^{-6}	14
E-Re30	30000	0.12	0.515	1.000 10^{-6}	19

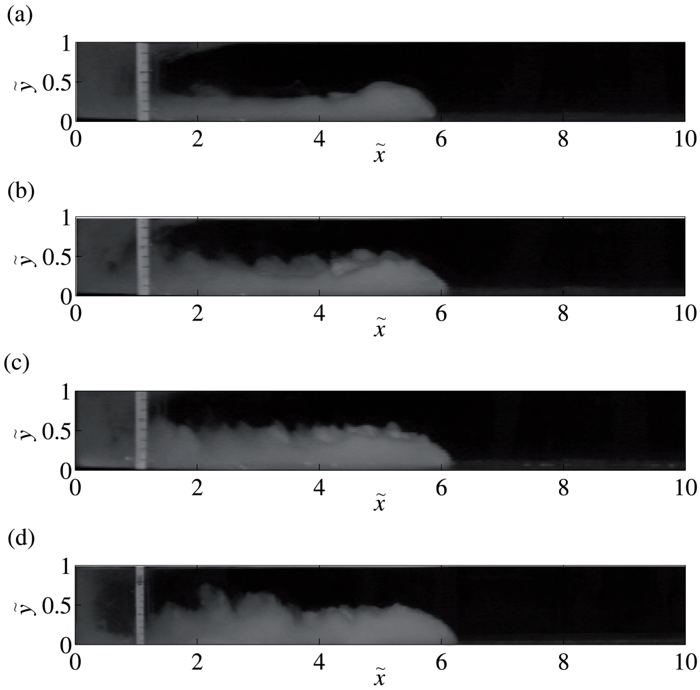

Figure 3: Images captured during the laboratory experiments at $\widetilde{t} = 11$ (a)$Re = 1000$; (b)$Re = 5000$; (c)$Re = 10000$; (d)$Re = 30000$.

5. Results and discussion

5.1. General considerations

2D and 3D numerical results are presented in this section and compared with experimental results obtained in the same conditions. The main dynamics of lock-release gravity currents can be described as essentially two-dimensional, since the buoyancy force driving the motion predominantly acts along the $x-y$ plane. The three-dimensional features developing in the spanwise direction are generally neglected for the description of the main flow and averaged quantities along the cross-sectional direction of homogeneity are considered (spanwise-averaged quantities are indicated with the symbol $\langle\ \rangle$) [12, 13, 15, 14, 18]. The spanwise averaging is performed on all 3D numerical data. The dimensionless density field, $\widetilde{\rho}$, is defined as

$$\widetilde{\rho}(x,y,z,t) = \frac{\rho_m(x,y,z,t) - \rho}{\rho_m^0 - \rho} \tag{20}$$

The interface between the gravity current and the ambient fluid is defined through the analysis of the spanwise averaged density fields, $\langle\widetilde{\rho}\rangle$, and the iso-density level corresponding to $\langle\widetilde{\rho}\rangle = 0.02$ is here selected as threshold for the interface, in agreement with previous studies [45, 14, 18, 4, 46].
Results relative to the instantaneous dimensionless front position $\widetilde{x}_f$ versus dimensionless time $\widetilde{t}$ and to density and velocity fields are analysed.
Dimensionless time $\widetilde{t}$ and front position $\widetilde{x}_f$ are defined as:

$$\widetilde{x}_f = \frac{x_f - x_0}{x_0},\ \widetilde{t} = \frac{t\sqrt{g\beta C_0 H}}{x_0} \tag{21}$$

being x_f the dimensional front position. From the experimental point of view, the front position is defined as the position of the foremost point of the nose of the gravity current along the streamwise direction. From the numerical point of view, the definition of the front position differs between 2D and 3D numerical simulations. As for 2D numerical simulations, the definition of the front position is the same as in the experiments, i.e. the location of the foremost point of the nose of the current. As for 3D numerical simulations, the definition of the front position is inferred from the analysis of the spanwise-averaged density fields. The front velocity u_f is defined as $u_f = \frac{dx_f}{dt}$ and it represents the velocity of the front of the gravity current.

As well known [26], three phases can be distinguished in the evolution of the gravity current: the slumping, the self-similar and the viscous phase. After the removal of the gate dividing the dense and the ambient fluids, the dense current forms and starts to propagate downstream at constant velocity, developing the flow regime known as the slumping phase. During the following self-similar phase, buoyancy forces are balanced by inertial forces, the current decelerates, and the front position evolves according to the theoretical power law of $\widetilde{t}^{2/3}$. As the current continues to decelerate, viscous forces can become important and the viscous regime can occur, characterized by a decrease of the front velocity proportionally to $\widetilde{t}^{-4/5}$. The first phase occurs for $x_0 \leq x_f \leq 9\ x_0$, the second phase for $9\ x_0 < x_f \leq l_{vis}$, the third phase for $x_f > l_{vis}$. The ratio of the viscous length l_{vis} to the lock's length x_0 is defined as [26]:

$$\frac{l_{vis}}{x_0} = \left(R \times Re \right)^{\frac{2}{7}} \tag{22}$$

The ratio l_{vis}/x_0 is reported in Table 2 for the considered cases. The gravity current with $Re = 1000$ develops the viscous phase directly after the slumping phase and the self-similar regime is not developed.

During the propagation of the current, ambient fluid is entrained into the body of the dense current, changing both the density field and the main features of the flow. These changes affect deeply the dynamics of the current as a whole. For this reason, the entrainment of ambient fluid during the propagation of the dense current is investigated too. Mixing between the dense current and the ambient fluid is usually modelled by the use of the entrainment parameter, E, which represents a dimensionless vertical velocity of ambient fluid directed into the dense current. In fact, during its propagation, the gravity current entrains ambient fluid, with a consequent increase in volume of the dense current and a decrease of its concentration. Following the approach of [2, 14, 18] it is possible to define the entrainment parameter as the ratio between the entrainment velocity, W_e, and a velocity scale [47]:

$$E(t) = \frac{W_e(t)}{2\ U(t)} \tag{23}$$

where $U(t)$ is defined as $x_f(t)/t$ and it represents a bulk velocity of the flow used as velocity scale. The entrainment velocity is defined as:

$$W_e(t) = \frac{\Delta V(t)}{\Delta t}\frac{1}{S(t)} \tag{24}$$

where $\Delta V(t)$ is the variation in volume of the dense current delimited by the iso-density level $\langle \widetilde{\rho} \rangle = 0.02$, at each t, with respect to the initial volume of the lock fluid V_0 at the initial time t_0; Δt is the time interval from t_0 to t; $S(t)$ is the area of the interface dividing the dense and the ambient fluids. Since the entrainment parameter is related to the variation in volume of the dense current, it can be affected by the definition of the interface dividing the dense and the ambient fluids. As mentioned before, in the present work the iso-density threshold $\langle \widetilde{\rho} \rangle = 0.02$ was chosen to define the interface of the dense current, so that most of the fluid with a dimensionless density greater than zero is considered as part of the dense current, in agreement with previous studies [44, 4, 14, 18] . Variations of this threshold in the range of $0.01 \leq \langle\widetilde{\rho}\rangle \leq 0.05$ do not significantly affect E. Further discussions on the dependency of E on the threshold used to define the current can be found in [14]. The entrainment parameter is analysed in the following, and results obtained from 3D simulations are compared with the values of E observed during the laboratory experiments.

Results relative to 2D and 3D numerical simulations are analysed separately in the following subsections.

5.2. 2D simulations

The dimensionless front position $\widetilde{x}_f$ versus dimensionless time $\widetilde{t}$ is shown in Fig. 4 for the cases considered in Table 2. The linear behaviour, typical for the slumping phase, is revealed by both numerical and experimental results. For the cases $Re = 1000$ and $Re = 5000$ (Figs. 4a and 4b) the numerical front position decelerates at about $\widetilde{x_f} \sim 6x_0$, indicating that the inertial and viscous forces start to affect the motion and that a transition in regime occurs, in agreement with [26]. For the cases $Re = 10000$ and $Re = 30000$ (Figs. 4c and 4d) a constant value of the front velocity is observed up to $\widetilde{x}_f = 8$. On the other hand, experimental results do not show any visible deceleration up to the distance of $9x_0$, indicating that, during the laboratory experiments, the transition to the following flow regime occurs slightly after the prediction of [26].

The density and velocity fields of the gravity currents at dimensionless time $\widetilde{t} = 11$, versus dimensionless abscissa $\widetilde{x}$ and ordinate $\widetilde{y}$ ($\widetilde{x} = x/x_0$, $\widetilde{y} = y/H$),

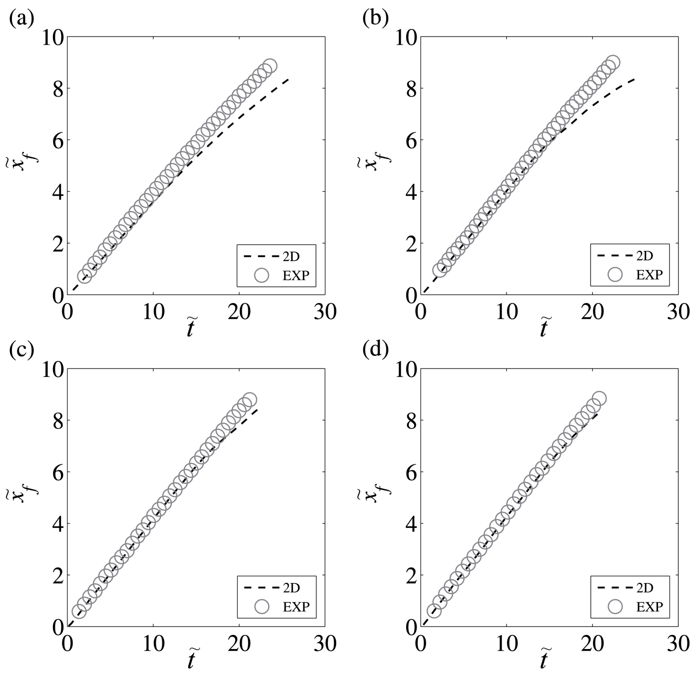

Figure 4: $\widetilde{x}_f$ versus $\widetilde{t}$. Dashed lines refer to the two-dimensional simulations and circles mark the laboratory experiments. (a)$Re = 1000$; (b)$Re = 5000$; (c)$Re = 10000$; (d)$Re = 30000$.

are shown in Figs. 5 and 6, respectively. Density and velocity fields change thoroughly with Re and their shape corresponds qualitatively to the experimental gravity current shape shown in Fig. 3 for the four cases considered in Table 2.

For $Re = 1000$ the interface between the dense and the ambient fluids is smooth and well defined (Figs. 3a, 5a, 6a), corresponding to a strong horizontal stratification of the dense fluid, visible in the body of the current (Fig. 5a). The gravity current is characterized by a rounded head followed by a horizontal body and a tail region with a decreasing thickness.

For $Re = 5000$ the interface of the current becomes irregular, as can be clearly observed (Figs. 3b, 5b, 6b).

For $Re = 10000$ and $Re = 30000$ the presence of irregularities at the interface characterize the behaviour of the dense currents, due to the development of Kelvin-Helmholtz instabilities. In these high-Re cases, mixing between the dense current and the ambient fluid occurs and it is clearly observable in Figs. 3c-3d, 5c-5d and 6c-6d.

The increase of the complexity of the flow field with the increase of Re is highlighted in Fig. 6. High intensities of the velocity module are visible in the head and in the body of the dense currents, while lower values are observed in the tail regions. Finally, peaks of the velocity module are found in correspondence of the Kelvin-Helmholtz billows (Figs. 6b-d).

5.3. 3D simulations

Three-dimensional numerical simulations were performed for $Re = 1000$, $Re = 5000$ and $Re = 10000$. The dimensionless front position $\widetilde{x}_f$ is shown in Fig. 7. A satisfying agreement can be observed between the numerical

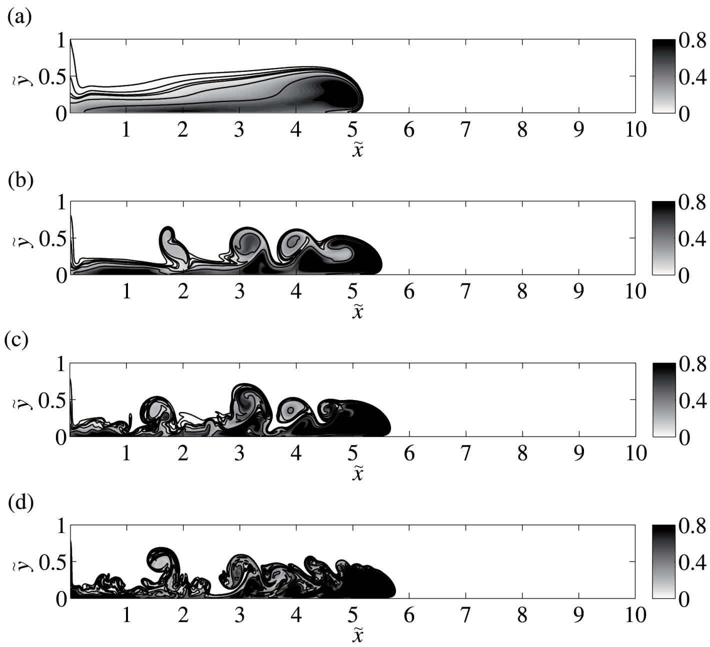

Figure 5: Dimensionless density field of two-dimensional simulations at $\widetilde{t} = 11$ (a)$Re = 1000$; (b)$Re = 5000$; (c)$Re = 10000$; (d)$Re = 30000$. Iso-density contours are draft for $\widetilde{\rho} = 0.02$, $\widetilde{\rho} = 0.05$, $\widetilde{\rho} = 0.08$, $\widetilde{\rho} = 0.10$, $\widetilde{\rho} = 0.20$ and $\widetilde{\rho} = 0.50$.

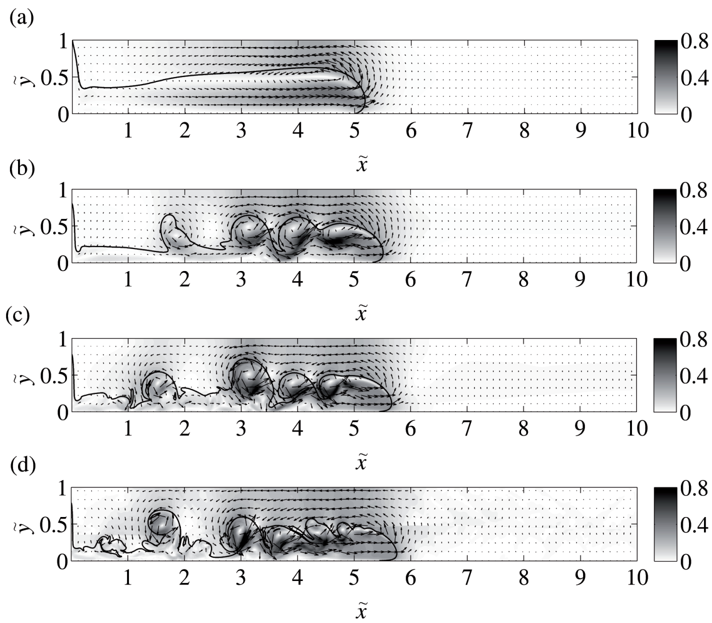

Figure 6: Dimensionless velocity field of two-dimensional simulations at $\widetilde{t} = 11$ (a)$Re = 1000$; (b)$Re = 5000$; (c)$Re = 10000$; (d)$Re = 30000$. Contourmaps refer to the velocity module intensity. Quantities are made dimensionless with u_b. The Iso-density level $\widetilde{\rho} = 0.02$ is also draft to show the interface of the current.

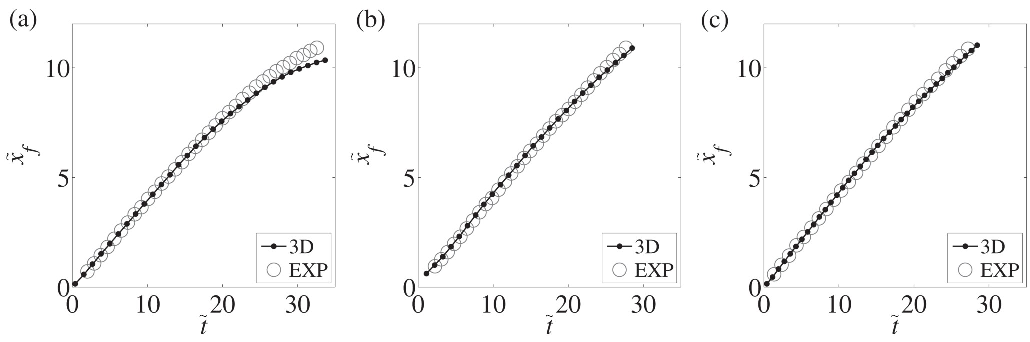

Figure 7: $\widetilde{x}_f$ versus $\widetilde{t}$. Solid lines with dots refer to the three-dimensional simulations and circles mark the laboratory experiments. (a)$Re = 1000$; (b)$Re = 5000$; (c)$Re = 10000$.

and the experimental front positions of the gravity currents. The slumping regime is well reproduced by the 3D simulations for all the considered Re. The behaviour of $Re = 1000$ is similar to that obtained with the 2D simulations: with respect to experimental results, numerical results move the start of the viscous phase up, in agreement with [26]. The development of the three phases of the gravity current's evolution is highlighted in Figs. 8a-8b, where bi-logarithmic plots $\widetilde{x}_f$ versus $\widetilde{t}$ are shown. Numerical results are plotted in Fig. 8a, experimental results in Fig. 8b. For $Re = 1000$, the sudden transition from the slumping phase to the viscous phase, without the development of the self-similar phase, is confirmed in both the simulation and the experiment (although in the laboratory experiment the decrease in velocity of the front was observed with a slight delay if compared to the simulation, at a distance of about 10 x_0). For $Re = 5000$ and $Re = 10000$ the slumping phase is followed by the self-similar phase and the start of the viscous regime is observed too.

Following [48], the front velocity u_f made dimensionless with u_b is plotted

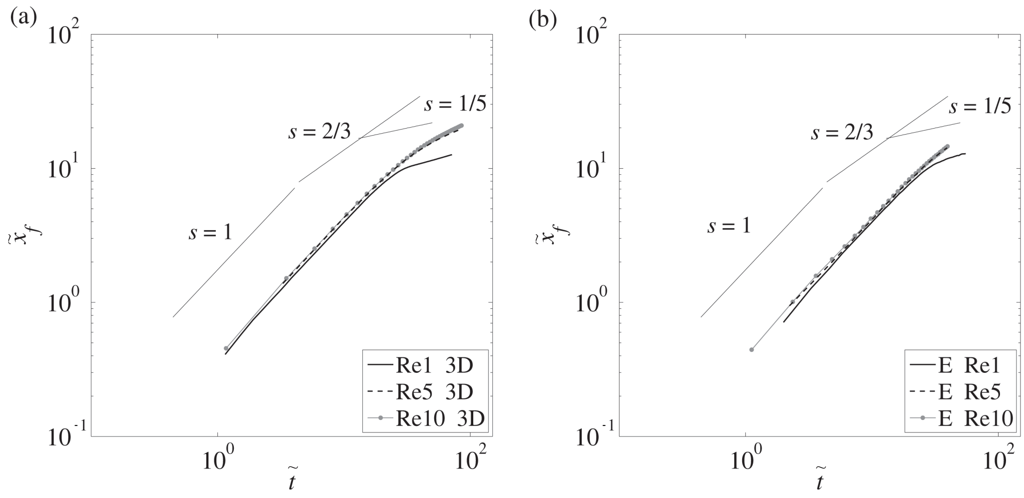

Figure 8: $\widetilde{x}_f$ versus $\widetilde{t}$ in a bilogarithmic scale. Solid lines refer to $Re = 1000$, dashed lines indicate $Re = 5000$ and grey lines with dots mark $Re = 10000$. (a)3D simulations; (b)laboratory experiments.

versus $\widetilde{x_f}$ in Fig. 9, in a bi-logarithmic scale. The theoretical trends of the slumping, the self-similar and the viscous phases are also reported with solid, dashed and dotted lines, respectively. The passage through the different flow regimes is highlighted by the use of $\widetilde{x_f}$ as abscissa, which causes abrupt changes in trend of the lines marking the different phases. The ratio u_f/u_b is commonly known as Froude numbed F_D, evaluated considering the initial height of the dense current h_0 [48, 49]. The mean value of F_D during the slumping phase increases with Re and assumes the values of 0.39, 0.41 and 0.42 for the $Re = 1000$, $Re = 5000$ and $Re = 10000$ cases, respectively, in agreement with values observed in literature [48, 49, 10, 4, 14]. The constant velocity phase is clearly detected in Fig. 9 and a mean value of $F_D = 0.41$ for the present simulations is marked by the solid line. After the dense current has travelled for a distance of about 6.5 lock-lengths, an abrupt decelera-

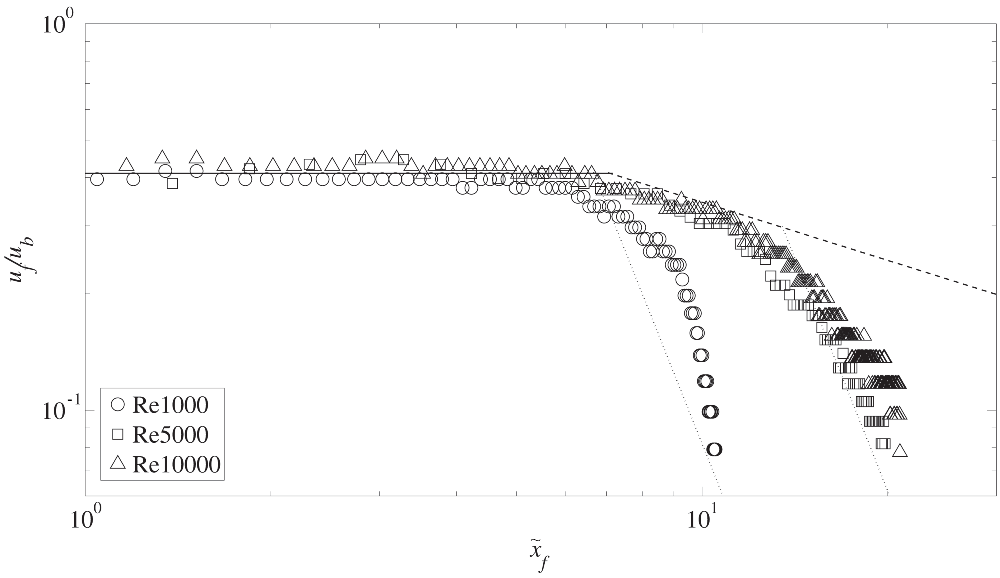

Figure 9: Log-log plot of $\widetilde{u}_f$ versus $\widetilde{x_f}$. Solid line indicates the slumping phase and refers to $F_D = 0.41$, dashed line marks the self-similar phase and dotted lines refer to the viscous phase. Circles, squares and triangles indicate $Re = 1000$, $Re = 5000$ and $Re = 10000$ 3D simulations, respectively.

tion of the front and the transition to the viscous phase can be observed for $Re = 1000$, in agreement with [26]. The self-similar phase is also developed in the other simulations and the passage to the viscous phase is observed at $\widetilde{x_f} \sim 11.5$ for $Re = 5000$ and $\widetilde{x_f} \sim 14$ for $Re = 10000$. This indicates a better agreement with [26] of 3D simulations than 2D simulation.

The spanwise-averaged density fields obtained by the three-dimensional simulations are shown in Fig. 10. The increase of Re affects the density fields, as already seen for 2D simulations, with the arise of turbulent patterns at the interface between the two fluids and a more complex behaviour in the internal part of the dense current. Kelvin-Helmholtz billows develop due to shear stress at the interface, but in 3D numerical simulations they appear less strong and less coherent than in the 2D simulations. This fact was observed also in [10], where a stronger effect of the Kelvin-Helmholtz billows in 2D numerical simulations rather than in 3D ones was found, because of the break of the spanwise coherence by turbulent disturbances developing along the third dimension. In fact, although Kelvin-Helmholtz billows are known to be mainly two dimensional vortices occupying all the spanwise direction, they can decay during the propagation of the current and their coherence can be broken and overridden by turbulent disturbances developing along the spanwise direction. This process, obviously, can not occur in 2D simulations and thus the strength of Kelvin-Helmholtz billows remains well active during all the propagation of the current.

Figure 11 shows the dimensionless density field of Re10-3D at different times and at different positions along the spanwise direction ($\widetilde{z} = H/2$ and $\widetilde{z} = H/4$). The time evolution of the turbulent structures arising in the current can be followed by looking at the panels from the top to the bottom of the figure. On the other hand, the same instant at different spanwise locations can be observed by looking at Fig. 11 from left to right. Strong and coherent billows develop at the rear part of the head of the dense current which can be detected at all $\widetilde{z}$-planes. Except for these rollers at the head of the current, different shape and size of the turbulent structures are generally detected with varying $\widetilde{z}$. For example, a well-defined KH billow can be observed to grow and develop at $\widetilde{x} \sim 2$, at the plane $\widetilde{z} = H/2$ (Figs. 11 a and c); this structure loses its coherence at the following times (Fig. 11 e) and disappear at $\widetilde{t} = 19$ (Fig. 11 g). The same billow, at the plane $\widetilde{z} = H/4$,

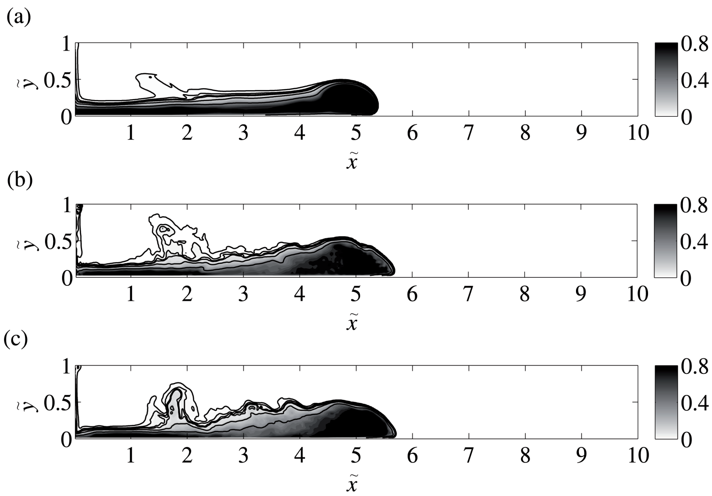

Figure 10: Spanwise-averaged dimensionless density field of three-dimensional simulations at $\widetilde{t} = 11$ (a)$Re = 1000$; (b)$Re = 5000$; (c)$Re = 10000$. Iso-density contours are draft for the same levels as in Fig. 5.

is less defined and less strong since $\widetilde{t} = 8$ (Fig. 11 b); it breaks up earlier than in $\widetilde{z} = H/2$ (Fig. 11 d), and at $\widetilde{t} = 16$ it is already hardly discernible (Fig. 11 f). This indicates the destabilization of the large billows due to the spanwise instabilities and the arise of turbulent structures with varying shape and size depending on $\widetilde{z}$ and $\widetilde{t}$.

The three-dimensional density iso-surfaces are shown in Fig. 12 for simulations Re1-3D, Re5-3D and Re10-3D. The presence of an increased amount of three-dimensional irregularities at the interface is clearly observed with the increase of Re. For $Re = 1000$ (Fig. 12a) the density iso-surface sharply divides the dense and the ambient fluids: the interface is smooth and continuous. Furthermore, the field is essentially two-dimensional, with the absence of interface discontinuities along the spanwise direction. For $Re = 5000$ (Fig. 12b) the three-dimensionality of the flow arises: lobes and clefts structures

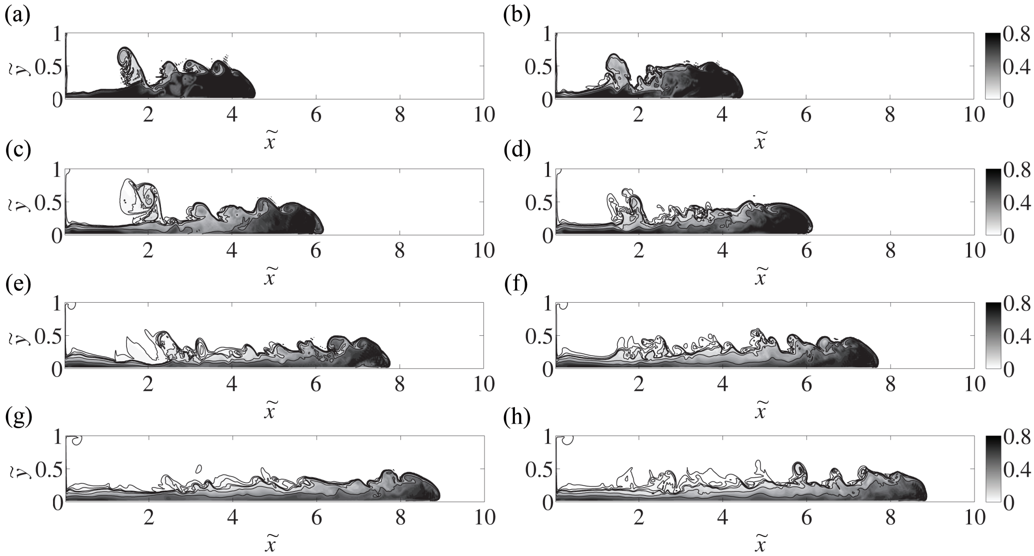

Figure 11: Dimensionless density field of Re10-3d at fixed planes in the spanwise direction corresponding to $\widetilde{z} = H/2$ (left panels) and $\widetilde{z} = H/4$ (right panels), at different times: (a)-(b) $\widetilde{t} = 8$; (c)-(d)$\widetilde{t} = 12$; (e)-(f)$\widetilde{t} = 16$; (g)-(h)$\widetilde{t} = 19$. Iso-density contours are draft for the same levels as in Fig. 5.

develop under the nose of the dense current and propagate upstream along the current's head, until they break up and generate chaotic turbulent patterns along the spanwise direction. Finally, for $Re = 10000$ (Fig. 12c) the flow is clearly three-dimensional, with much more fully developed lobes and clefts structures than in $Re = 5000$.

Following [50, 10, 11], the time evolution of the lobes and clefts instabilities is shown in Fig.13, by the visualization of the top view of the front advancement of the current at a $(\widetilde{x}, \widetilde{z})$-plane close to the bottom of the domain, defined by the iso-density contour $\widetilde{\rho} = 0.02$. At the beginning of the simulations the front is almost continuous along the spanwise direction, but when

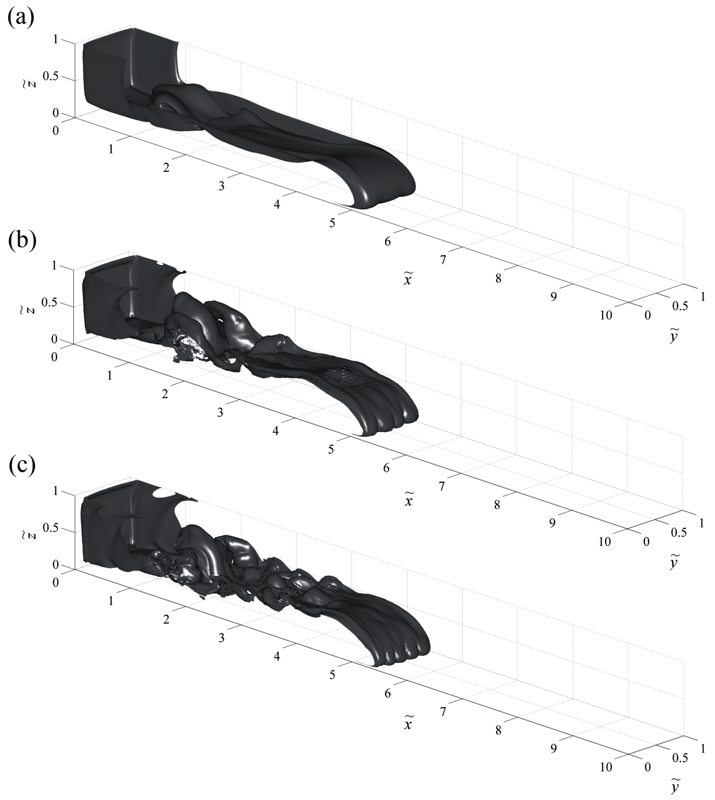

Figure 12: Density iso-surfaces ($\widetilde{\rho} = 0.02$) of three-dimensional simulations at $\widetilde{t} \sim 11$ (a)$Re = 1000$; (b)$Re = 5000$; (c)$Re = 10000$.

it reaches $\widetilde{x} \sim 3$, disturbances develop, quickly evolving in well-defined lobes and clefts structures. Consequently, the front of the current varies along the spanwise direction due to the presence of lobes and clefts instabilities which evolve in time, shifting along the spanwise direction, rearranging, merging and dividing. A complex pattern can be observed in Fig.13, with several merging of cleft and splitting of lobes. As expected, the complexity of these dynamics increases with increasing Re (Fig.13 c) and decreases as the time advances. In fact, it is known that the mean length scale of the lobes and clefts patterns, depends on the instantaneous Reynolds of the flow [50, 10], $Re_F = \frac{u_f h_H}{\nu}$, that is defined with the time-varying characteristics of the flow at the head of the dense current: the front velocity u_f, and the height of the head of the current $\widetilde{h_H}$ [10, 11]. Following the approach of [50, 11], the number of lobes, n, and their size, $\widetilde{\lambda}$, can be derived by observing Fig. 13 and counting. For each simulation, two times for each phase of spreading were selected and analysed. The times selected and the relative variables are resumed in Table 3. The dependence of the mean lobe size, $\widetilde{\lambda}$, versus the instantaneous Reynolds number, Re_F, is shown in Fig.14, where the empirical relation derived by [50] is also draft:

$$\frac{\widetilde{\lambda}}{\widetilde{h_H}} = 7.4 Re_F^{-0.39\pm0.02} \tag{25}$$

Data referring to the different simulations are marked with different symbols, while colors are used to indicate the different flow regimes at which the current is flowing. As can be observed in Fig.14, the present results are in agreement with the prediction of [50](the curve which best fits our data goes as $Re_F^{-0.408}$), with an inverse proportion between the local Reynolds number and the mean lobes' amplitude. The simulation Re1-3D is characterized by a low Reynolds number and thus the number of lobes developing in the spanwise direction is small (Fig.13 and Table 3) and the lobes' amplitude is larger than the other cases (Fig.14). With increasing Re, the flow becomes turbulent, the number of lobes detected increases and their mean amplitude decreases, in agreement with [10] (in ascending order, stars, squares and circles in Fig.14). Further, advancing in time, Re_F decreases, because the current passes from the slumping regime, up to the viscous regime, and thus spanwise instabilities reduce in number and lobes become larger (in order:

Table 3: Quantitative information for the evaluation of the number and the amplitude of the lobes and clefts instabilities.

Simulation	$\widetilde{x_f}$	$\widetilde{t}$	u_f/u_b	$\widetilde{h_H}$	n	$\widetilde{\lambda}/\widetilde{h_H}$	Re_F	phase
Re1-3D	3.9	10.0	0.40	0.52	3	0.65	204	slump.
Re1-3D	6	15.3	0.38	0.45	4	0.56	167	slump.
Re1-3D	9	25.3	0.24	0.27	3	1.24	64	visc.
Re1-3D	10	30.6	0.14	0.20	2	2.5	28	visc.
Re5-3D	4.7	11.0	0.40	0.55	3	0.61	1094	slump.
Re5-3D	6	14.2	0.41	0.51	3	0.65	1044	slump.
Re5-3D	9.2	23.0	0.33	0.48	3	0.69	786	self-sim.
Re5-3D	10.9	28.5	0.30	0.44	3	0.76	669	self-sim.
Re5-3D	15.1	47.1	0.18	0.39	3	0.86	342	visc.
Re5-3D	17.1	60.3	0.13	0.37	2	1.37	235	visc.
Re10-3D	4.0	9.3	0.43	0.51	5	0.39	2184	slump.
Re10-3D	6.2	14.4	0.41	0.51	5	0.39	2084	slump.
Re10-3D	9.0	22.2	0.33	0.42	4	0.60	1390	self-sim.
Re10-3D	11.3	28.4	0.31	0.44	4	0.57	1370	self-sim.
Re10-3D	15.0	44.0	0.21	0.39	4	0.65	824	visc.
Re10-3D	17.0	55.3	0.16	0.37	3	0.90	576	visc.

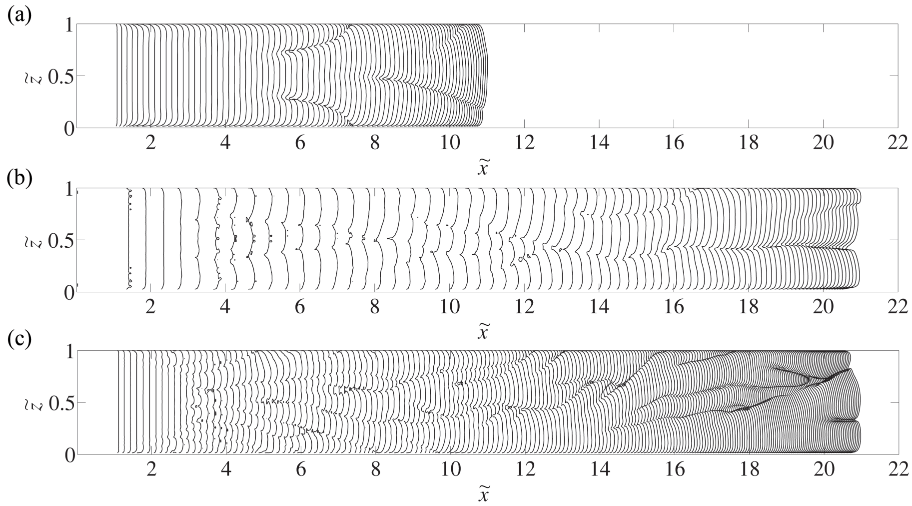

Figure 13: Time evolution of the lobes and clefts instabilities inferred from a top-view of the iso-density contour $\widetilde{\rho} = 0.02$ on a $(\widetilde{x}, \widetilde{z})$-plane near the bottom of the domain: (a)$Re = 1000$; (b)$Re = 5000$; (c)$Re = 10000$.

full-black symbols, empty symbols and full-grey symbols in Fig.14). A similar trend was already observed by [11].

The entrainment parameter, E, is evaluated for the 3D numerical simulations and compared to the values observed during the laboratory experiments. The entrainment is known to be dependent on a bulk Froude number, Fr_b, and a bulk Reynolds number, Re_b, [2, 51] respectively defined as:

$$Fr_b = \frac{U}{\sqrt{g'_m \frac{H}{2}}} \tag{26}$$

$$Re_b = \frac{U \frac{H}{2}}{\nu} \tag{27}$$

where g'_m is an averaged value of the reduced gravity assumed at the beginning (g') and at the end (g'_f) of each simulation. Furthermore, it was

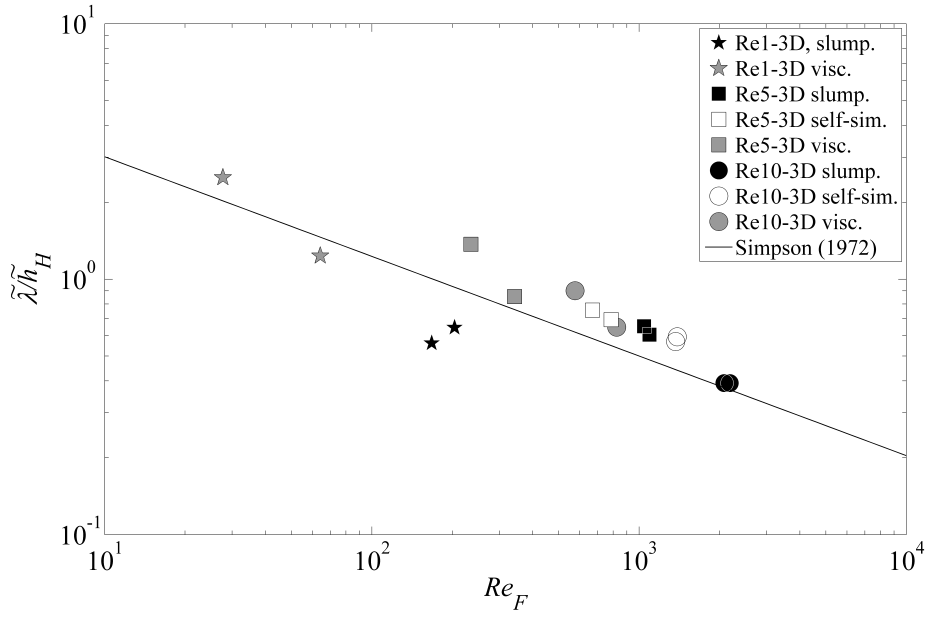

Figure 14: Lobes amplitude made dimensionless with the height of the head of the current versus the local Reynolds number. Stars mark the Re1-3D simulation, squares indicate the Re5-3D simulation and circles are for Re10-3D simulation. Full-black symbols indicate the slumping regime, full-grey symbols refer to the self-similar regime and empty symbols are for the viscous regime. The empirical prediction of [50] (Eq. 25) is also shown as black solid line.

observed that E depends on the length of the path travelled by the dense current [2, 18]. Thus, for each simulation and each experiment, the value of E after the dense current has travelled for 10 lock-lengths is considered here, which is about the maximum length of the path travelled by the current in the $Re = 1000$ case, before it stops. The values of E versus Fr_b and E versus Re_b are plotted in Figs. 15a and 15b, respectively. As expected, the values of Fr_b and Re_b increase with the increase of Re and, in agreement with literature, E increases as a consequence [2, 51, 14, 18]. This trend is verified both in the numerical simulations and in the experiments. The order of magnitude of E is 10^{-2} for the cases with $Re = 5000$, $Re = 10000$ and $Re = 30000$ and is slightly lower for $Re = 1000$ ($E \sim 0.008$). E evaluated in the simulations is fairly comparable with the one observed in the experiments and, in addition, is in agreement with previous evaluations of the entrainment in lock-release gravity currents [14, 18, 5, 46]. Entrainment evaluations of LES and laboratory experiments of lock-release gravity currents presented in [14] are also plotted in Fig. 15 for comparison purposes (grey symbols). Also for these data, E was evaluated after the dense current has travelled for the same distance used in the present experiments. The values of Re in the dataset of [14] ranged between 34000 and 68000, so they were higher than the ones considered in the present study ($1000 \leq Re \leq 30000$). For this reason, the values of E evaluated with the dataset of [14] are slightly higher than those of the present study, and are close to the point referring to E-Re30. However, the order of magnitude of 10^{-2} is observed in both studies. Entrainment parametrizations derived by previous studies on steady and unsteady gravity currents are also reported in Fig. 15(a). The relations of [52, 53, 51] derive from the analysis of laboratory experiments and field measurements of density currents fed by a constant discharge of dense water, i.e., steady gravity currents. These currents are generally characterized by larger Froude numbers ($Fr_b \geq 1$) and lower Reynolds numbers than the ones observed in lock-release flows. When $Fr_b < 1$, these parametrizations predict values of E ranging between $10^{-4} - 10^{-3}$, if not null as in [52], and thus are unsuitable to be used in applications simulating unsteady flows. On the other hand, the entrainment parametrizations of [5, 54] were proposed to take

into account the entrainment in two-layer shallow-water models simulating lock-release rectangular cross-section and axisymmetric gravity currents, i.e. unsteady gravity currents, as the ones of the present study. For this reason, for $Fr_b < 1$, they supply values of E comparable to the present entrainment evaluations and are in agreement with the entrainment parameters observed for subcritical lock-exchange gravity currents [5, 46, 14, 18].
This fact confirms the capability of the Lattice Boltzmann Method to correctly reproduce not only the advancement in time of the front propagation of the gravity current and its main features, but also its increase in volume due to the entrainment of ambient fluid.

6. Conclusion

In this paper the ability of the Lattice Boltzmann Method (LBM) in reproducing the fundamental features of lock-exchange gravity currents was assessed. Both 2D and 3D numerical simulations were considered at different Reynolds numbers: $Re = 1000$, $Re = 5000$, $Re = 10000$ and $Re = 30000$. Laboratory experiments were performed and compared with numerical results, showing a good agreement. The different phases of the gravity current evolution were revealed at a satisfactory extent. In the low-Reynolds cases ($Re = 1000$ and $Re = 5000$) the numerical results tended to move up the onset of the inertial and viscous phases. In particular, for $Re = 1000$ numerical results showed the abrupt transition from the slumping to the viscous phase, without developing the inertial phase. The effect of the increase of the Reynolds number, mainly consisting in the decrease of the characteristic

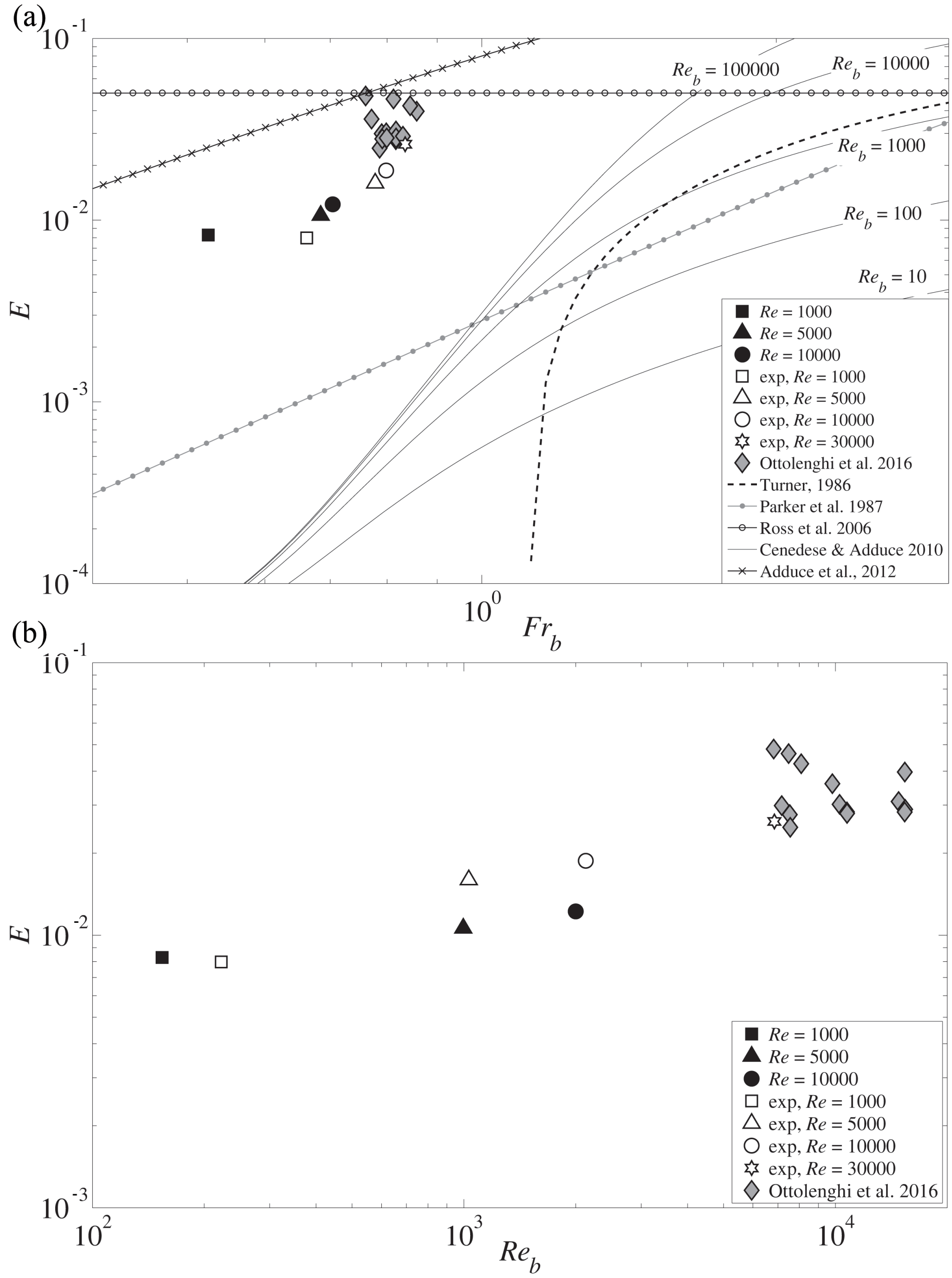

Figure 15: Entrainment parameter evaluated in 3D numerical simulations (full black symbols) and laboratory experiments (empty symbols): (a) E versus Fr; (b) E versus Re. Entrainment evaluations of lock-release gravity currents presented in [14] are also plotted with grey symbols. Entrainment parametrizations for both steady and unsteady gravity currents are finally draft: [52] (dashed line); [53] (grey line with dots); [54] (solid line with circles); [51] depending on Re_b (black solid lines); [5] (solid line with crosses)

length-scale of the turbulent structures, was highlighted both by 2D and 3D numerical simulations. By means of the latter, turbulent structures along the spanwise direction, as well as lobes and clefts structures were clearly highlighted. The time evolution of lobes and clefts instabilities was analysed, revealing an increase of the amount of lobes detected in the flow with the increase of Re_F, in agreement with literature [50, 10, 11]. Finally, through the evaluation of the entrainment parameter, the capability of the numerical model to correctly reproduce also the increase in volume of the dense current during its propagation was demonstrated. In conclusion, the LBM can be considered as a valid tool for the investigation on gravity currents.

Acknowledgments

The authors acknowledge financial support through the Italian national research grant "Hydroelectric energy by osmosis in coastal areas," PRIN 2010-2011.

References

[1] J. E. Simpson, Gravity currents: In the environment and the laboratory, Cambridge University Press, 1997.

[2] C. Cenedese, C. Adduce, Mixing in a density-driven current flowing down a slope in a rotating fluid., J. Fluid Mech. 604 (2008) 369–388.

[3] L. Ottolenghi, C. Cenedese, C. Adduce, Entrainment in a dense current flowing down a rough sloping bottom in a rotating fluid, J. Phys. Oceanogr. 47 (3) (2017) 485–498.

[4] H. Nogueira, C. Adduce, E. Alves, M. Franca, Analysis of lock-exchange gravity currents over smooth and rough beds, J. Hydraul. Res. 51 (4) (2013) 417–431.

[5] C. Adduce, G. Sciortino, S. Proietti, Gravity currents produced by lock exchanges: Experiments and simulations with a two-layer shallow-water model with entrainment, J. Hydraul. Eng.-ASCE 138 (2) (2012) 111–121.

[6] M. La Rocca, C. Adduce, G. Sciortino, A. B. Pinzon, Experimental and numerical simulation of three-dimensional gravity currents on smooth and rough bottom, Phys. Fluids 20 (10) (2008) 106603.

[7] M. La Rocca, C. Adduce, G. Sciortino, A. B. Pinzon, M. A. Boniforti, A two-layer, shallow-water model for 3d gravity currents, J. Hydraul. Res. 50 (2) (2012) 208–217.

[8] V. Lombardi, C. Adduce, G. Sciortino, M. L. Rocca, Gravity currents flowing upslope:laboratory experiments and shallow water simulations, Phys. Fluids 27 (1) (2015) 016602.

[9] C. Härtel, E. Meiburg, F. Necker, Analysis and direct numerical simulation of the flow at a gravity-current head. part 1. flow topology and front speed for slip and no-slip boundaries, J. Fluid Mech. 418 (2000) 189–212.

[10] M. Cantero, J. Lee, S. Balachandar, M. García, On the front velocity of gravity currents, J. Fluid Mech. 586 (2007) 1–39.

[11] M. Cantero, J. Lee, S. Balachandar, M. García, High-resolution simulations of cylindrical density currents, J. Fluid Mech. 590 (2007) 437–469.

[12] S. Ooi, G. Constantinescu, L. Weber, Numerical simulations of lock-exchange compositional gravity current, J. Fluid Mech. 635 (2009) 361–388.

[13] T. Tokyay, G. Constantinescu, E. Meiburg, Lock-exchange gravity currents with a high volume of release propagating over a periodic array of obstacles, J. Fluid Mech. 672 (2011) 570–605.

[14] L. Ottolenghi, C. Adduce, R. Inghilesi, V. Armenio, F. Roman, Entrainment and mixing in unsteady gravity currents, J. Hydraul. Res. 54 (5) (2016) 541–557.

[15] A. Dai, C. Ozdemir, M. Cantero, S. Balachandar, Gravity currents from instantaneous sources down a slope, J. Hydraul. Eng. 138 (3) (2012) 237–246.

[16] A. Dai, Gravity currents propagating on sloping boundaries, J. Hydraul. Eng. 139 (6) (2013) 593–601.

[17] A. Dai, High-resolution simulations of downslope gravity currents in the acceleration phase, Phys. Fluids 27 (7) (2015) 076602.

[18] L. Ottolenghi, C. Adduce, R. Inghilesi, F. Roman, V. Armenio, Mixing in lock-release gravity currents propagating up a slope, Phys. Fluids 28 (5) (2016) 056604.

[19] L. Ottolenghi, C. Adduce, F. Roman, V. Armenio, Analysis of the flow in gravity currents propagating up a slope, Ocean Modelling 115 (2017) 1–13.

[20] S. Succi, The lattice Boltzmann equation: for fluid dynamics and beyond, Oxford university press, 2001.

[21] C. K. Aidun, J. R. Clausen, Lattice-boltzmann method for complex flows, Annual review of fluid mechanics 42 (2010) 439–472.

[22] Z. Guo, B. Shi, C. Zheng, A coupled lattice bgk model for the boussinesq equations, International Journal for Numerical Methods in Fluids 39 (4) (2002) 325–342.

[23] M. La Rocca, C. Adduce, V. Lombardi, G. Sciortino, R. Hinkelmann, Development of a lattice boltzmann method for two-layered shallow-water flow, Int. J. Numer. Meth. Fl. 70 (8) (2012) 1048–1072.

[24] M. La Rocca, P. Prestininzi, C. Adduce, G. Sciortino, R. Hinkelmann, Lattice boltzmann simulation of 3d gravity currents around obstacles, International Journal of Offshore and Polar Engineering 23 (3) (2013) 178–185.

[25] P. Prestininzi, M. La Rocca, R. Hinkelmann, et al., Comparative study of a boltzmann-based finite volume and a lattice boltzmann model for shallow water flows in complex domains, International Journal of Offshore and Polar Engineering 24 (03) (2014) 161–167.

[26] J. Rottman, J. Simpson, Gravity currents produced by instantaneous

releases of a heavy fluid in a rectangular channel, J. Fluid Mech. 135 (1983) 95–110.

[27] S. Hou, J. Sterling, S. Chen, G. Doolen, A lattice boltzmann subgrid model for high reynolds number flows, arXiv preprint comp-gas/9401004.

[28] R. Benzi, S. Succi, M. Vergassola, The lattice boltzmann equation: theory and applications, Physics Reports 222 (3) (1992) 145–197.

[29] B. Cushman-Roisin, J.-M. Beckers, Introduction to geophysical fluid dynamics: physical and numerical aspects, Vol. 101, Academic Press, 2011.

[30] S. Chen, G. D. Doolen, Lattice boltzmann method for fluid flows, Annual review of fluid mechanics 30 (1) (1998) 329–364.

[31] V. K. BIRMAN, B. A. BATTANDIER, E. MEIBURG, P. F. LINDEN, Lock-exchange flows in sloping channels, Journal of Fluid Mechanics 577 (2007) 5377.

[32] M. I. Cantero, S. Balachandar, M. H. Garca, D. Bock, Turbulent structures in planar gravity currents and their influence on the flow dynamics, Journal of Geophysical Research: Oceans 113 (C8) (2008) 2156–2202.

[33] M. Bouzidi, M. Firdaouss, P. Lallemand, Momentum transfer of a boltzmann-lattice fluid with boundaries, Physics of Fluids (1994-present) 13 (11) (2001) 3452–3459.

[34] G. Wellein, T. Zeiser, G. Hager, S. Donath, On the single processor performance of simple lattice boltzmann kernels, Computers and Fluids 35 (89) (2006) 910 – 919, proceedings of the First International Conference for Mesoscopic Methods in Engineering and Science.

[35] A. G. Shet, S. H. Sorathiya, S. Krithivasan, A. M. Deshpande, B. Kaul, S. D. Sherlekar, S. Ansumali, Data structure and movement for lattice-based simulations, Physical Review E 88 (1) (2013) 013314.

[36] A. Peters, S. Melchionna, E. Kaxiras, J. Lätt, J. Sircar, M. Bernaschi, M. Bison, S. Succi, Multiscale simulation of cardiovascular flows on the ibm bluegene/p: Full heart-circulation system at red-blood cell resolution, in: Proceedings of the 2010 ACM/IEEE International Conference for High Performance Computing, Networking, Storage and Analysis, IEEE Computer Society, 2010, pp. 1–10.

[37] M. Bernaschi, M. Bisson, T. Endo, S. Matsuoka, M. Fatica, Petaflop biofluidics simulations on a two million-core system, in: High Performance Computing, Networking, Storage and Analysis (SC), 2011 International Conference for, IEEE, 2011, pp. 1–12.

[38] J. Tölke, M. Krafczyk, Teraflop computing on a desktop pc with gpus for 3d cfd, International Journal of Computational Fluid Dynamics 22 (7) (2008) 443–456.

[39] M. Bernaschi, L. Rossi, R. Benzi, M. Sbragaglia, S. Succi, Graphics processing unit implementation of lattice boltzmann models for flowing soft systems, Phys. Rev. E 80 (2009) 066707.

doi:10.1103/PhysRevE.80.066707.
URL https://link.aps.org/doi/10.1103/PhysRevE.80.066707

[40] C. Obrecht, F. Kuznik, B. Tourancheau, J.-J. Roux, A new approach to the lattice boltzmann method for graphics processing units, Computers and Mathematics with Applications 61 (12) (2011) 3628 – 3638.

[41] M. Bernaschi, M. Bisson, M. Fatica, S. Melchionna, S. Succi, Petaflop hydrokinetic simulations of complex flows on massive gpu clusters, Computer Physics Communications 184 (2) (2013) 329–341.

[42] J. Habich, T. Zeiser, G. Hager, G. Wellein, Performance analysis and optimization strategies for a {D3Q19} lattice boltzmann kernel on nvidia {GPUs} using {CUDA}, Advances in Engineering Software 42 (5) (2011) 266 – 272, {PARENG} 2009.

[43] M. L. Sheely, Glycerol viscosity tables, Industrial & Engineering Chemistry 24 (9) (1932) 1060–1064.

[44] H. Nogueira, C. Adduce, E. Alves, M. Franca, Image analysis technique applied to lock-exchange gravity currents, Meas. Sci. Technol. 24 (4) (2013) 047001.

[45] L. Ottolenghi, C. Adduce, R. Inghilesi, F. Roman, V. Armenio, Large eddy simulation of gravity currents moving on up-sloping boundaries, in: River Flow 2014: International conference on Fluvial Hydraulics, Lausanne, Switzerland, 3-5 September 2014, 2014, p. 189.

[46] H. Nogueira, C. Adduce, E. Alves, M. Franca, Dynamics of the head of gravity currents, Environ. Fluid Mech. 14 (2014) 519–540.

[47] J. Turner, Buoyant convection from isolate sources. Buoyancy Effects In Fluids, Cambridge University Press, 1973.

[48] B. M. Marino, L. P. Thomas, P. F. Linden, The front condition for gravity currents, J. Fluid Mech. 536 (2005) 49–78.

[49] J. Shin, S. Dalziel, P. Linden, Gravity currents produced by lock exchange, J. Fluid Mech. 521 (2004) 1–34.

[50] J. E. Simpson, Effects of the lower boundary on the head of a gravity current, J. Fluid Mech. 53 (4) (1972) 759–768.

[51] C. Cenedese, C. Adduce, A new parameterization for entrainment in overflows., J. Phys. Oceanogr. 40 (8) (2010) 1835–1850.

[52] J. S. Turner, Turbulent entrainment: the development of the entrainment assumption and its application to geophysical flows., J. Fluid Mech. 170 (1986) 431–471.

[53] G. Parker, M. Garcia, Y. Fukushima, W. Yu, Experiments on turbidity currents over an erodible bed, J. Hydraul. Res. 25 (1) (1987) 123–147.

[54] A. Ross, S. Dalziel, P. Linden, Axisymmetric gravity currents on a cone, J. Fluid Mech. 565 (2006) 227–253.